Fermi-Level Tuning of Epitaxial Sb_2Te_3 Thin Films on Graphene by Regulating Intrinsic Defects and Substrate Transfer Doping

Yeping Jiang,[1,2] Y. Y. Sun,[3] Mu Chen,[1,2] Yilin Wang,[1] Zhi Li,[1] Canli Song,[1,2] Ke He,[1] Lili Wang,[1] Xi Chen,[2]
Qi-Kun Xue,[1,2] Xucun Ma,[1,*] and S. B. Zhang[3,†]

[1]*Institute of Physics, Chinese Academy of Sciences, Beijing 100190, China*
[2]*State Key Lab of Low-Dimensional Physics, Department of Physics, Tsinghua University, Beijing 100084, China*
[3]*Department of Physics, Applied Physics, and Astronomy, Rensselaer Polytechnic Institute, Troy, New York 12180, USA*
(Received 22 August 2011; published 10 February 2012)

High-quality Sb_2Te_3 films are obtained by molecular beam epitaxy on a graphene substrate and investigated by *in situ* scanning tunneling microscopy and spectroscopy. Intrinsic defects responsible for the natural *p*-type conductivity of Sb_2Te_3 are identified to be the Sb vacancies and Sb_{Te} antisites in agreement with first-principles calculations. By minimizing defect densities, coupled with a transfer doping by the graphene substrate, the Fermi level of Sb_2Te_3 thin films can be tuned over the entire range of the bulk band gap. This establishes the necessary condition to explore topological insulator behaviors near the Dirac point.

The discovery of three-dimensional topological insulators (TIs) in group V chalcogenides, whose topological surface states (SSs) host two-dimensional helical Dirac fermions (DFs), has spurred tremendous interests in this class of materials as a potential vehicle for the exotic physical phenomena to exist only in DFs [1–6]. While Bi_2Te_3 and Bi_2Se_3 have been intensively studied in recent years [7–14], the study of Sb_2Te_3 in the context of its TI behavior is still rare [15,16]. While all these chalcogenide TIs have a simple SS band structure, consisting of a single Dirac cone in the surface Brillouin zone, Sb_2Te_3 stands out for its unique advantages over Bi_2Te_3 and Bi_2Se_3; for example, the Dirac point lies well-detached from the bulk band edges [16,17] to allow better measurement and manipulation of the DFs.

All available TIs are heavily populated by intrinsic defects. By introducing a significant amount of free carriers, these defects pin the Fermi level to the bulk band edges to shadow the electronic and spintronic responses of the DFs [5,18,19]. As such, defect control for fine-tuning the Fermi level inside the bulk band gap, especially at the exact charge neutrality point, has become an important and challenging issue in TI studies [7–9,20–23]. Previously, we established [24] a technique to control intrinsic defects in molecular beam epitaxy (MBE)-grown Bi_2Te_3 thin films by regulating substrate temperature. Both *n*-type and *p*-type Bi_2Te_3 can be obtained without extrinsic doping. Such a simple technique, however, does not work for Bi_2Se_3 (mostly *n*-type) and Sb_2Te_3 (mostly *p*-type). So far, *p*-type Bi_2Se_3 thin films can only be obtained by introducing a high concentration of extrinsic dopants [8]. There has been no *n*-type Sb_2Te_3 reported, unless one δ dopes Sb_2Te_3 by depositing a submonolayer cesium on the surface of a thin film [16].

In this Letter, we show that the difficulty with Sb_2Te_3 film is resolved by the MBE growth of Sb_2Te_3 thin films on the graphene substrate without the extrinsic δ layer. There exists a special growth temperature, T_c, at which the concentration of the holes reaches a minimum. By experimental determination of such a condition in conjunction with a transfer doping by the substrate, the Fermi level of Sb_2Te_3 can now be tuned to coincide with the Dirac point for films of five quintuple layers or thicker. Our combined scanning tunneling microscopy (STM) and spectroscopy (STS) and density functional theory (DFT) calculation identify Sb vacancies (V_{Sb}) as the primary source of *p*-type conductivity for samples grown at low temperatures and Sb-on-Te antisites (Sb_{Te}) as those for samples grown at high temperatures. These findings are consistent with the observation of T_c at which the total concentration of the two acceptor defects reaches a minimum.

Our experiment was performed under an ultrahigh vacuum (base pressure $< 1 \times 10^{-10}$ Torr) in a combined low-temperature STM and MBE chamber. An *n*-doped 6H-SiC (0001) substrate was used. The surface of the SiC, upon graphitization, was covered by a graphene bilayer [25]. During the growth, high-purity Sb and Te (both 99.9999%) were codeposited onto the substrate from Knudsen cells. After the growth, the Sb_2Te_3 samples were transferred to an STM stage kept at 4.8 K, where the STM images and STS spectra (dI/dV) were taken. The STS spectra were acquired using a standard lock-in technique with a bias modulation of 1 mV_{rms} at 987.5 Hz.

The mechanism for the MBE growth of Sb_2Te_3 is more complex than that of Bi_2Se_3 [25,26] and Bi_2Te_3 [24,27]. During the growth of Sb_2Te_3, both Sb and Te fluxes are dominated by molecular species, mainly Sb tetramers (Sb_4) and Te dimers (Te_2). This is different from growing

Bi_2Se_3 and Bi_2Te_3, where Bi is mainly in the atomic form. A high substrate temperature and a low beam flux are required to avoid Sb clustering and the formation of structural defects due to the low mobility of Sb_4. In addition, the sticking coefficient of the Sb_4 on graphene is lower than that on Sb_2Te_3. At a fixed beam flux, the substrate temperature must be lower than the threshold T_0 for Sb_2Te_3 nucleation. After the nucleation stage, however, the temperature can be increased to improve the film quality. Thus, a two-step procedure was used. The Knudsen cell temperatures, T_{Sb} and T_{Te}, were kept at 330 and 225 °C, respectively, which yield a Te-rich growth condition with a nominal Te/Sb flux ratio (θ) of $\sim$10 and a low growth rate of $\sim$0.2 quintuple layers (QL) per minute. At this beam flux, T_0 is $\sim$190 °C. The two-step growth temperatures T_1 and T_2 are thus set at $\sim$190 and 200–250 °C, respectively.

Figure 1(a) shows a typical STM image of the Sb_2Te_3 film. A regular terrace step of $\sim$1.01 nm or 1 QL clearly indicates a layer-by-layer growth mode. The terraces are atomically flat and of good crystallinity, as evidenced by the atomic resolution image [inset of Fig. 1(a)]. The (111) lattice constant is measured to be $\sim$0.426 nm. The layer-by-layer growth mode is further confirmed by the evolution of the quantum well states (QWSs) in the thin film. This can be seen in Fig. 1(b), where a series of dI/dV spectra are taken on films of 1–8 QL. The layered crystal structure of Sb_2Te_3 is shown in Fig. S1(a) of the Supplemental Material [28]. Within the Tersoff-Hamann approximation

[29], dI/dV spectra correspond to the local density of states (LDOS) for the film. The peaks on the low-energy side of the LDOS (marked by arrows) correspond to the QWS in the bulklike valence band (BVB), whereas the steps in the high-energy side correspond to the QWS in the bulklike conduction band (BCB). The separation between the QWS decreases with increasing film thickness. The energy difference between the highest BVB QWS and the lowest BCB QWS is related to the bulk energy gap. It decreases from $\sim$900 meV at 1 QL to $\sim$400 meV at 8 QL, as can be seen in Fig. 1(b). More details about characterizing the QWS states by STS are provided in the Supplemental Material (Fig. S2) [28].

For a thick film ($\sim$ 50 QL), the LDOS spectrum in Fig. 1(c) shows a bulk gap of $\sim$300 meV. The oscillations due to QWSs in the BVB can still be clearly observed with a peak-to-peak distance of $\sim$23 meV. In the energy range of the bulk gap, the SS can be probed, showing a V-shaped spectrum with the zero-conductance point at $\sim$100 meV, corresponding to the Dirac point (E_D) of the SS [17]. The observation of the zero-conductance point in the bulk gap is direct evidence that the Dirac point on the Sb_2Te_3 surface is well-detached from the bulk band edges. The position of E_D [$\sim$ 100 meV in Fig. 1(c)] is insensitive to the growth parameters for thick films, for which the Fermi level is pinned around the BVB edge. This result reinforces the notion that both Sb_2Te_3 films and bulk samples are p-type [15,16], which has hindered the use of photoemission techniques, a major tool for the investigation of the physical properties of the TIs [7,9].

Five types of defects under various growth conditions are observed. Figures 2(a) and 2(b) show the STM images for samples grown at $\sim$190 and $\sim$230 °C, respectively, with $\theta = \sim$10. Four types of defects (labeled I, II, IV, and V) can be seen. At an even more Te-rich condition (e.g., $\theta = \sim$20), another type of defects (labeled III) is observed, as shown in Fig. 2(c). Defects I, II, IV, and V are all acceptors, as judged by the Dirac point position in the corresponding LDOS spectra (see Supplemental Material Fig. S3 [28]).

Figure 2(d) shows high-resolution STM images for the observed defects. The corresponding positions of these defects, as shown in Figs. 2(e) and 2(f), are assigned by measuring their lateral registries with respect to the top-layer Te atoms and by considering the spatial distribution of their STM features. The chemical bonding in Sb_2Te_3 is similar to that in Bi_2Te_3 and Bi_2Se_3 [10] and can be approximated by strongly interacting $pp\sigma$ chains of atomic p orbitals [30] with the order Te1-Sb-Te2-Sb-Te1, as shown in Fig. 2(f). A defect is expected to perturb the electronic states predominantly along three equivalent, 120°-apart $pp\sigma$ chains passing the defect, resulting in three spots at surface atoms terminating the chains. The center joining the three spots is the lateral position of the defect. A surface Te-site defect (i.e., defect IV) is an
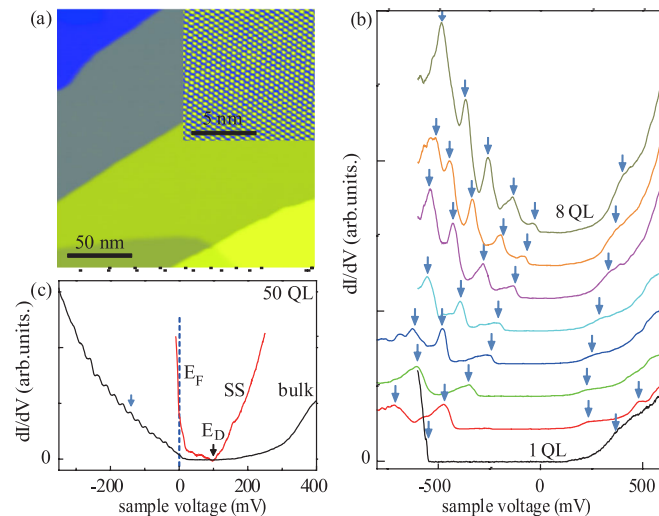

FIG. 1 (color online). (a) STM image of a Sb_2Te_3 film less than 10 QL (V_{bias} = 5.0 V, I = 50 pA). The inset is an atomic resolution image ($-$ 1.0 V, 50 pA). Bright spots correspond to surface Te. (b) dI/dV spectra (0.3 V, 50 pA) of films from 1 to 8 QL. Arrows indicate the energies of bulklike QWS. (c) dI/dV spectra of bulk (0.3 V, 50 pA) and SSs (0.25 V, 200 pA) on a 50 QL Sb_2Te_3 film.
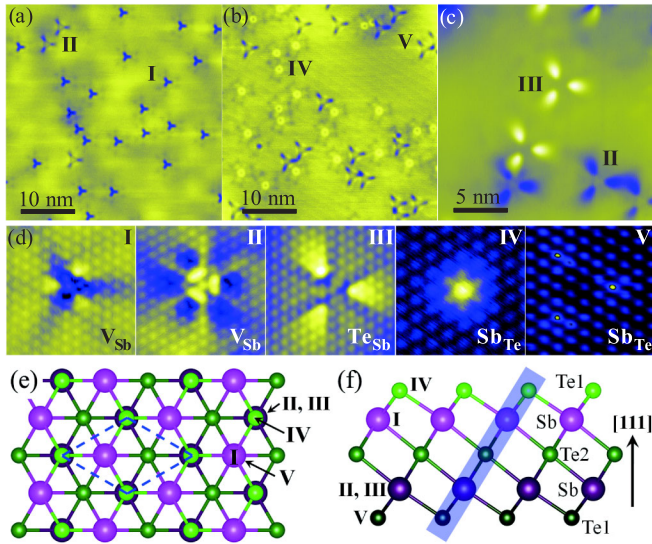
FIG. 2 (color online). (a)–(c) Large-area STM images for various defects, labeled from I to V. Tunneling conditions: (a) 1.0 V, 50 pA; (b) 1.0 V, 50 pA; and (c) 0.4 V, 50 pA. (d) High-resolution STM images for defects I to V. Tunneling conditions: (I) 0.2 V, 100 pA; (II) 0.1 V, 100 pA; (III) 0.2 V, 100 pA; (IV) −0.5 V, 50 pA; and (V) −1.0 V, 50 pA. (e),(f) Top and side views of $Sb_2Te_3(111)$ showing positions of the defects. The dashed frame is the surface unit cell. The shaded region is a Te1-Sb-Te2-Sb-Te1 chain in a single QL. Te and Sb atoms are denoted by small (green) and large (pink) spheres, respectively. Note that, looking from the top, I is above V and IV is above II and III.
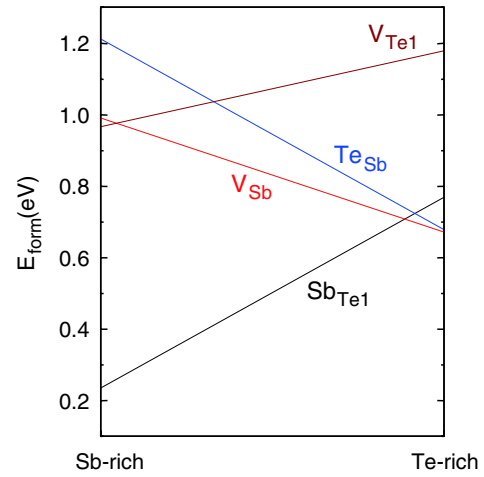

FIG. 3 (color online). Calculated intrinsic defect formation energy under various growth conditions: the Te-rich condition corresponds to the chemical potential of Te (μ_{Te}) set to that of bulk Te, whereas the Sb-rich condition corresponds to μ_{Sb} set to that of bulk Sb, with the constraint $2\mu_{Sb} + 3\mu_{Te}$ equal to the total energy per formula bulk Sb_2Te_3.

exception for which only one spot should be seen. Using this argument, we identify that defect I is centered on a Sb site in the second layer, defects II and III are on Sb sites in the fourth layer, and defects IV and V are on Te sites in the first and fifth layers, respectively. More details on defect identification are given in the Supplemental Material (Fig. S1) [28]. In Fig. 2(d), defects I, II, IV, and V show depression at positive bias and protrusion at negative bias, implying that they are electron acceptors, in accordance with the LDOS measurement using STS {Fig. S3(c) in the Supplemental Material [28]}. On the other hand, defect III shows an opposite contrast, for example, to defect II [see Fig. 2(c)], even though they are on the same atomic site, implying that defect III is an electron donor. Thus, we may attribute defects I and II to Sb vacancies (V_{Sb}), defect III to a Te-on-Sb antisite (Te_{Sb}), and defects IV and V to Sb_{Te1} in different atomic layers, as illustrated in Fig. 2(f).

The occurrence of these defects is intimately related to growth temperature T and flux θ: V_{Sb} only exists at relatively low T and disappears above ~200 °C. Te_{Sb} coexists with V_{Sb} at low T (< 200 °C) and high θ. Sb_{Te1} appears at ~200 °C. Sb_{Te2} has not been observed for 190 °C < T < 250 °C, indicating that it has a higher formation energy than Sb_{Te1}.

The defect assignments above are verified by DFT calculations, performed using the VASP code [31]. The generalized gradient approximation [32] was used for the exchange-correlation functional. Core electrons were represented by the projector augmented wave potentials [33]. Plane waves with a cutoff energy of 250 eV were used as the basis set. A (4 × 4 × 1) 240-atom supercell with lattice constants (a = 4.264 Å and c = 30.458 Å) was used to model the defects. A single special k point at (7/24, 1/12, 1/4) was used to sample the Brillouin zone. Defect formation energies were calculated following the formalism in Ref. [34].

Figure 3 shows the calculated formation energy of possible intrinsic defects in Sb_2Te_3. At a strong Te-rich growth condition, V_{Sb} is the lowest-energy defect. When the system becomes less Te-rich, which could be a result of increased substrate temperature [24], Sb_{Te1} becomes the lowest-energy defect in agreement with our experiment. Our calculations confirmed that both defects are acceptors. The lack of Sb_{Te2} in our experiment can be explained because it is less stable than Sb_{Te1} by 0.2 eV. The lack of V_{Te} can also be explained by its high formation energy. In addition, at a highly Te-rich condition corresponding to higher θ, Te_{Sb} is only slightly higher in energy than V_{Sb}, in line with the coexistence of Te_{Sb} with V_{Sb} in Fig. 2(c).

We are unable to obtain Sb_2Te_3 samples in which the Te_{Sb} donor dominates. A too-high θ would degrade the sample morphology. To compensate for intrinsic acceptors, carriers of opposite sign must be introduced. In this regard, the n-doped graphene substrate can serve as an electron donor. Figure 4(a) shows the thickness dependence of E_D with respect to E_F. Between 4 and 5 QL, the two levels cross, implying an n-to-p–type conversion. The substrate
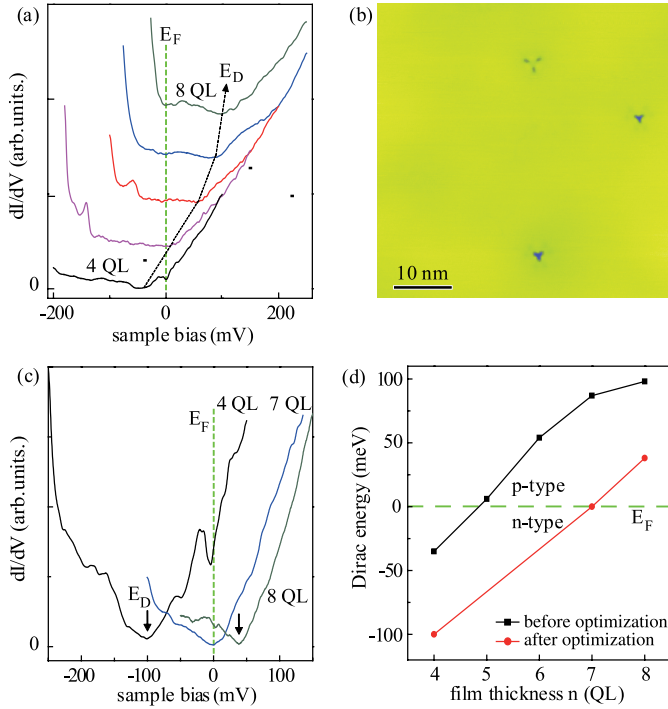
FIG. 4 (color online).   (a) Thickness-dependent SS spectra of Sb$_2$Te$_3$ films from 4 to 8 QL. The spectra are shifted vertically for clarity. (b) STM image (1.0 V, 50 pA) of the optimized sample. (c) SS spectra for 4, 7, and 8 QL optimized films. (d) Evolution of E_D with film thickness.

transfer doping effect decays with film thickness, with the critical thickness at about ~8 QL for this set of samples, above which E_D approaches the bulk value.

With the knowledge on the defect formation, the thickness of the n-type region can be further increased by reducing the density of intrinsic acceptors to enable a wider range of Fermi-level tuning. Figure 3 predicts that, at the transition region between V_{Sb} and Sb$_{Te1}$, the acceptor density is the lowest. Experimentally, we determined that this corresponds to the growth condition: $\theta = \sim 10$ and $T_2 = \sim 200\,^\circ$C, at which the amount of intrinsic defects is greatly reduced. Figure 4(b) shows that the defect density is on the order of $\sim 1.2 \times 10^{11}/$cm^2, compared to, for example, $\sim 1.7 \times 10^{12}/$cm^2 for other samples. Accordingly, Fig. 4(d) shows consistently that E_D is shifted downwards by ~60 meV. In particular, E_D is around -100 meV at 4 QL; E_D nearly coincides with E_F at 7 QL; and E_D is above E_F at 8 QL, as shown in Fig. 4(c), signaling the transition to a p-type region. These results demonstrate that E_F can be controlled in the energy range of ± 100 meV around E_D in our MBE samples while minimizing the effects of intrinsic or extrinsic defects.

In summary, by a combined STM-STS experiment and DFT calculation, we identify major intrinsic defects in MBE-grown Sb$_2$Te$_3$ on a graphene substrate and explain the p-type behavior of the undoped films. We show that, by combining substrate n doping with intrinsic defect control,

one could tune the Fermi level in Sb$_2$Te$_3$ thin films to across nearly the whole band gap region of bulk Sb$_2$Te$_3$. This paves the way for further study of the TI behavior in large-gap Sb$_2$Te$_3$: for example, due to the helical nature of TI SSs, the spin direction with respect to the momentum changes sign for states below and above E_D [35]. Thus, the Fermi surface of the SS may undergo a spin-texture reversion where the n-p transition takes place. In films with both electron and hole pockets of the DFs, exciton condensation may also be observed [4].

*Corresponding author.
  xcma@aphy.iphy.ac.cn
†Corresponding author.
  zhangs9@rpi.edu

[1] M. Z. Hasan and C. L. Kane, Rev. Mod. Phys. **82**, 3045 (2010).
[2] X.-L. Qi and S.-C. Zhang, Rev. Mod. Phys. **83**, 1057 (2011).
[3] L. Fu and C. L. Kane, Phys. Rev. Lett. **100**, 096407 (2008).
[4] B. Seradjeh, J. E. Moore, and M. Franz, Phys. Rev. Lett. **103**, 066402 (2009).
[5] A. M. Essin, J. E. Moore, and D. Vanderbilt, Phys. Rev. Lett. **102**, 146805 (2009).
[6] X.-L. Qi, R. Li, J. Zang, and S.-C. Zhang, Science **323**, 1184 (2009).
[7] Y. L. Chen *et al.*, Science **325**, 178 (2009).
[8] D. Hsieh *et al.*, Nature (London) **460**, 1101 (2009).
[9] Y. Xia *et al.*, Nature Phys. **5**, 398 (2009).
[10] H. J. Zhang *et al.*, Nature Phys. **5**, 438 (2009).
[11] P. Cheng *et al.*, Phys. Rev. Lett. **105**, 076801 (2010).
[12] T. Zhang *et al.*, Phys. Rev. Lett. **103**, 266803 (2009).
[13] Y. Zhang *et al.*, Nature Phys. **6**, 584 (2010).
[14] Z. Alpichshev *et al.*, Phys. Rev. Lett. **104**, 016401 (2010).
[15] D. Hsieh *et al.*, Phys. Rev. Lett. **103**, 146401 (2009).
[16] G. Wang *et al.*, Nano Res. **3**, 874 (2010).
[17] Y. P. Jiang *et al.*, Phys. Rev. Lett. **108**, 016401 (2012).
[18] X.-L. Qi, T. L. Hughes, and S.-C. Zhang, Phys. Rev. B **78**, 195424 (2008).
[19] Q. Liu *et al.*, Phys. Rev. Lett. **102**, 156603 (2009).
[20] J. G. Checkelsky *et al.*, Phys. Rev. Lett. **103**, 246601 (2009).
[21] J. Chen *et al.*, Phys. Rev. Lett. **105**, 176602 (2010).

[22] D.-X. Qu et al., Science **329**, 821 (2010).

[23] H. Peng et al., Nature Mater. **9**, 225 (2010).

[24] G. Wang et al., Adv. Mater. **23**, 2929 (2011).

[25] C. L. Song et al., Appl. Phys. Lett. **97**, 143118 (2010).

[26] G. Zhang et al., Appl. Phys. Lett. **95**, 053114 (2009).

[27] Y. Y. Li et al., Adv. Mater. **22**, 4002 (2010).

[28] See Supplemental Material at http://link.aps.org/supplemental/10.1103/PhysRevLett.108.066809 for the detailed crystal structure of this layered material.

[29] J. Tersoff and D. R. Hamann, Phys. Rev. B **31**, 805 (1985).

[30] S. K. Mishra and et al., J. Phys. Condens. Matter **9**, 461 (1997).

[31] G. Kresse and J. Furthmuller, Comput. Mater. Sci. **6**, 15 (1996).

[32] J. P. Perdew, K. Burke, and M. Ernzerhof, Phys. Rev. Lett. **77**, 3865 (1996).

[33] G. Kresse and D. Joubert, Phys. Rev. B **59**, 1758 (1999).

[34] S. B. Zhang and J. E. Northrup, Phys. Rev. Lett. **67**, 2339 (1991).

[35] S.-Y. Xu et al., Science **332**, 560 (2011).